PERGAMON

International Journal of Heat and Mass Transfer 42 (1999) 467–475

International Journal of HEAT and MASS TRANSFER

Numerical study of magneto-fluid-mechanic combined free-and-forced convection heat transfer

M. J. Al-Khawaja[a], R. K. Agarwal[b], R. A. Gardner[c,*]

[a] *Mechanical Engineering, Qatar University, Doha, Qatar*
[b] *Aerospace Engineering, Wichita State University, Wichita, KS 67260, U.S.A.*
[c] *Department of Mechanical Engineering, Washington University, St Louis, MO 63130, U.S.A.*

Received 30 December 1997; in final form 9 May 1998

Abstract

Fully-developed, laminar, steady, free-and-forced convection heat transfer in an electrically-conducting fluid flowing in an electrically-insulated, horizontal, circular pipe (with its wall subjected to a uniform heat flux) in a vertical, uniform, transverse magnetic field was solved numerically using several finite difference schemes for Grashof numbers from 0 to 10^6 and Hartmann numbers from 0 to 500. For high Hartmann numbers, a refinement of the mesh in the radial direction was necessary in the Hartmann boundary layer and relaxation techniques were needed to have a convergent solution. Velocity profiles, temperature profiles and local and average Nusselt numbers are reported for combined free-and-forced convection.

Nomenclature

a pipe radius [m]
B_0 magnetic field [T]
c specific heat [J kg^{-1} K^{-1}]
d pipe diameter [m]
Gr Grashof number, $g\beta a^4 q/kv^2$
h η mesh size
h_c heat transfer coefficient
H dimensionless axial field, $H_z/[u_m(\sigma\mu_f)^{1/2}]$
H^* normalized field, H/γ
i η-integer variable $1, 2, 3, \ldots, L-1$
j φ-integer variable $1, 2, 3, \ldots, K$
k thermal conductivity [W m^{-1} K^{-1}]
K maximum of j integer at $\Phi = \pi$
L maximum of i integer at $\eta = 1$
M Hartmann number, $B_0 a(\sigma/\mu_f)^{1/2}$
n iteration step $1, 2, 3, \ldots$
Nu Nusselt number, $h_c d/k$
Pr Prandtl number, $\mu_f c/k$
q wall heat flux, $k\,\partial T/\partial r$ at $r = a$
r radial coordinate [m]
r, φ, z polar coordinates
Re Reynolds number, $u_m d/v$
R_M magnetic Reynolds number, $\sigma\mu u_m a$
R_s RMS of residuals for s variable
T temperature [°C]
T_a area-average temperature [°C]
T_m bulk mixing-cup temperature [°C]
u dimensionless radial velocity, u_r/U^*
u_m mean axial velocity [m s^{-1}]
u_r radial velocity [m s^{-1}]
u_φ azimuthal velocity [m s^{-1}]
u_z axial velocity [m s^{-1}]
U^* reference velocity for radial and azimuthal directions, $a\sqrt{g\beta q/k}$ [m s^{-1}]
v dimensionless azimuthal velocity, u_φ/U^*
w dimensionless axial velocity, u_z/u_m
w^* normalized axial velocity, w/γ.

Greek symbols
β volumetric thermal expansion [K^{-1}]
γ dimensionless pressure gradient, $[(\partial P/\partial z)a^2]/u_m\mu_f$
η dimensionless radial coordinate, r/a
θ dimensionless temperature, $(T-T_a)/(aq/k)$
μ magnetic permeability [kg m A^{-2} s^{-2}]
μ_f dynamic viscosity [Ns m^{-2}]
v kinematic viscosity [m^2 s^{-1}]
ξ dimensionless axial vorticity

* Corresponding author.

0017–9310/98 $19.00
PII: S0017–9310(98)00172–0

ρ density [kg m^{-3}]
σ electrical conductivity [A V^{-1} m^{-1}]
φ angular coordinate
ψ dimensionless stream function
ω relaxation parameter.

1. Introduction

Considerable attention has been given to magnetohydrodynamic (MHD) flows since the beginning of this century. Significant applications have been reported such as the MHD generator, MHD flow meter, MHD pump and MHD marine propulsion. Some other quite promising applications are in the field of metallurgy such as MHD stirring of molten metal and magnetic-levitation casting. A very useful proposed application which involves MHD is the lithium cooling blanket in a nuclear fusion reactor [1]. With the high-temperature plasma contained in the reactor by means of a toroidal magnetic field, liquid lithium flows in channels (blankets) between the plasma and magnetic windings to absorb the thermal energy released by the fusion reaction. The proximity of the lithium blankets to the field coils means that the flow will be acted upon by extremely strong magnetic fields. Consequently, a knowledge of fundamental MHD interactions is necessary in order to determine pressure drops, heat transfer, etc., in channels or pipes situated at different angles to a magnetic field. One such fundamental flow is that a magneto-fluid-mechanic (MFM) pipe flow subjected to a transverse magnetic field with combined free-and-forced convection heat transfer. The laminar flow considered here is also the limiting case for turbulent flow at high Reynolds numbers (even 10^6 or higher) where high magnetic fields can damp out turbulent fluctuations and 'laminarize' the flow [2]. Lo [3, 4] investigated this laminar problem using a perturbation method which produced some details of the secondary flow but his results were limited to small values of the Hartmann number, $M = B_0 a\sqrt{\sigma/\mu_f}$. The present work extends this problem by solving the appropriate governing partial differential equations simultaneously to yield the stream function of the secondary flow, the induced magnetic field, streamwise and azimuthal velocity profiles, temperature distributions and local and average Nusselt numbers. For $Gr \leqslant 10^4$, the central difference scheme is employed. The modified third-order-accurate upwind scheme is applied in the convective terms for larger Grashof numbers up to 10^6. The Grashof number, $Gr = (g\beta a^4 q/kv^2)$, is based on the constant wall heat flux boundary conditions. In terms of the range of Hartmann numbers and Grashof numbers considered here, one could reach a Grashof number of 10^6 and a Hartmann number of 500 with the flow of a liquid metal such as mercury in a 6 cm diameter pipe, a wall heat flux of 1.0 kW m^{-2} and an applied magnetic field of 0.63 Tesla. Other liquid metals would have a similar range of parameters. Conducting fluids such as electrolytes would require a much higher applied field because their electrical conductivity is lower than that in liquid metals by several orders of magnitude.

2. Governing equations

From the assumptions that a constant vertical magnetic field is applied to electrically-conducting flow which is laminar, steady and fully-developed in an electrically-insulated, horizontal, circular pipe whose wall is subjected to a uniform heat flux, the dimensionless governing equations for forced convection MFM pipe flow can be cast into a coupled set of five partial differential equations [5, 6]. For most typical engineering applications, the magnetic Reynolds number, R_M, is much less than unity (unless the length scale is large as found in astrophysical applications) and the governing equations can be simplified due to the fact that the induced magnetic field is much smaller than the applied field. Only the interaction of the applied field and the fluid motion need to be taken into account. The momentum equations in the radial and azimuthal directions are cross differentiated and subtracted to eliminate the pressure gradient terms and the problem is cast in terms of the vorticity and stream functions in polar coordinates. Consult refs [3–6] for more details. Figure 1 shows the orientation of the pipe, field and cylindrical coordinate system.

2.1. Vorticity and stream function relationship

$$\nabla^2\psi = -\xi. \tag{1}$$

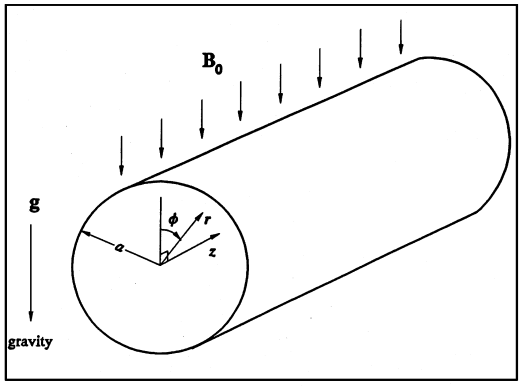

Fig. 1. Pipe cross-section showing coordinate system and orientation of the magnetic field.

2.2. Combined azimuthal and radial momentum equation

$$\nabla^2\xi+\frac{\sqrt{Gr}}{\eta}\left[\frac{\partial\psi}{\partial\eta}\frac{\partial\xi}{\partial\varphi}-\frac{\partial\psi}{\partial\varphi}\frac{\partial\xi}{\partial\eta}\right]=\sqrt{Gr}\left[\sin\varphi\frac{\partial\theta}{\partial\eta}+\frac{\cos\varphi}{\eta}\frac{\partial\theta}{\partial\varphi}\right]+M^2B(\xi,\psi) \quad (2)$$

where ξ is the axial vorticity of the secondary azimuthal and radial flow and

$$B(\xi,\psi)=\xi\sin^2\varphi-\cos 2\varphi\frac{\partial^2\psi}{\partial\eta^2}-\left[\frac{\sin 2\varphi}{\eta}\left(-\frac{\partial^2\psi}{\partial\eta\,\partial\varphi}+\frac{1}{\eta}\frac{\partial\psi}{\partial\eta}\right)\right].$$

2.3. Axial momentum equation

$$\nabla^2w^*+\frac{\sqrt{Gr}}{\eta}\left[\frac{\partial\psi}{\partial\eta}\frac{\partial w^*}{\partial\varphi}-\frac{\partial\psi}{\partial\varphi}\frac{\partial w^*}{\partial\eta}\right]+M\left[\frac{\sin\varphi}{\eta}\frac{\partial H^*}{\partial\varphi}-\cos\varphi\frac{\partial H^*}{\partial\eta}\right]=1. \quad (3)$$

2.4. Induction equation

$$\nabla^2H^*+M\left[\frac{\sin\varphi}{\eta}\frac{\partial w^*}{\partial\varphi}-\cos\varphi\frac{\partial w^*}{\partial\eta}\right]=0. \quad (4)$$

2.5. Energy equation

$$\nabla^2\theta-2w+\frac{Pr\sqrt{Gr}}{\eta}\left[\frac{\partial\psi}{\partial\eta}\frac{\partial\theta}{\partial\varphi}-\frac{\partial\psi}{\partial\varphi}\frac{\partial\theta}{\partial\eta}\right]=0. \quad (5)$$

The relation between w and w^* is given by

$$w=\frac{\pi w^*}{\int_0^1\int_0^{2\pi}w^*\eta\,\mathrm{d}\eta\,\mathrm{d}\varphi} \quad (6)$$

and the Laplacian ∇^2 operator in cylindrical coordinates by

$$\nabla^2=\frac{\partial^2}{\partial\eta^2}+\frac{1}{\eta}\frac{\partial}{\partial\eta}+\frac{1}{\eta^2}\frac{\partial^2}{\partial\varphi^2}$$

with the following dimensionless boundary conditions:

$w|_{\eta=1}=0$

from the no-slip condition,

$$v|_{\eta=1}=-\left.\frac{\partial\psi}{\partial\eta}\right|_{\eta=1}=0 \quad (7)$$

and

$$u|_{\eta=1}=\left.\frac{1}{\eta}\frac{\partial\psi}{\partial\varphi}\right|_{\eta=1}=0 \quad (8)$$

from the nonpermeable condition. From equations (7) and (8), one can deduce that it is sufficient to let

$$\psi|_{\eta=1}=0. \quad (9)$$

In addition, from the condition of zero wall electrical conductivity,

$$H|_{\eta=1}=0 \quad (10)$$

and from the condition of uniform heat flux at the wall

$$\left.\frac{\partial\theta}{\partial\eta}\right|_{\eta=1}=1. \quad (11)$$

It should also be kept in mind that all physical quantities are finite at the origin at $\eta=0$.

3. Difference equations

Figure 2 shows the general structure of the finite-difference mesh arrangement. Equations (1)–(5) are then discretized using the modified third-order upwind scheme [7] and the following equations are obtained, respectively:

$$G_1\psi_{i+1j}+G_2\psi_{i-1j}+G_3\psi_{ij+1}+G_3\psi_{ij-1}+G_0\psi_{ij}=-h^2\xi_{ij} \quad (12)$$

$$A_1x_{i+1j}+A_2\xi_{i-1j}+A_3\xi_{ij+1}+A_4\xi_{ij-1}+[A_0-M^2h^2\sin^2(j\delta\varphi)]\xi_{ij}=-S_{ij} \quad (13)$$

$$A_1w^*_{i+1j}+A_2w^*_{i-1j}+A_3w^*_{ij+1}+A_4w^*_{ij-1}+A_0w^*_{ij}=C_{ij} \quad (14)$$

$$G_1H^*_{i+1j}+G_2H^*_{i-1j}+G_3H^*_{ij+1}+G_3H^*_{ij-1}+G_0H^*_{ij}=D_{ij} \quad (15)$$

and

$$F_1\theta_{i+1j}+F_2\theta_{i-1j}+F_3\theta_{ij+1}+F_4\theta_{ij-1}+F_0\theta_{ij}=2h^2w_{ij}+Pr\,\mathscr{L}(\theta)_{ij} \quad (16)$$

where

$$G_1=1+\frac{1}{2i},\quad G_2=1-\frac{1}{2i},$$

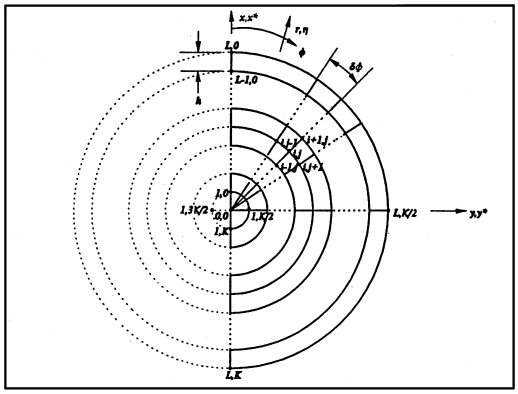

Fig. 2. Polar coordinate system showing η and φ mesh network.

$$G_3 = \frac{1}{(i\delta\varphi)^2}, \quad G_0 = -2\left[1+\frac{1}{(i\delta\varphi)^2}\right]$$

$$A_1 = G_1 - \frac{1}{6\delta\varphi}(3e-|e|), \quad A_2 = G_2 + \frac{1}{6\delta\varphi}(3e-|e|)$$

$$A_3 = G_3 - \frac{1}{6\delta\varphi}(3b+|b|), \quad A_4 = G_3 - \frac{1}{6\delta\varphi}(3b-|b|)$$

$$A_0 = G_0 - \frac{1}{6\delta\varphi}(b+|e|)$$

$$F_1 = G_1 - \frac{Pr}{6\delta\varphi}(3e-|e|), \quad F_2 = G_2 + \frac{Pr}{6\delta\varphi}(3e+|e|)$$

$$F_3 = G_3 + \frac{Pr}{6\delta\varphi}(3b+|b|), \quad F_4 = G_3 - \frac{Pr}{6\delta\varphi}(3b-|b|)$$

$$F_0 = G_0 - \frac{Pr}{6\delta\varphi}(|b|+|e|).$$

$$S_{ij} = -\frac{h\sqrt{Gr}}{2}\left[\sin(j\delta\varphi)\overline{\delta_\eta}(\theta)_{ij} + \frac{\cos(j\delta\varphi)}{i\delta\varphi}\overline{\delta_\varphi}(\theta)_{ij}\right] + M^2\left[\cos(2j\delta\varphi)\overline{\delta_\eta}^2(\psi)_{ij} + \frac{\sin(2j\delta\varphi)}{i}\left\{-\overline{\delta_\eta}\delta_\varphi(\psi)_{ij}\frac{1}{4\delta\varphi} + \frac{\overline{\delta_\eta}(\psi)_{ij}}{2i\delta\varphi}\right\}\right] - \mathscr{Z}(\xi)_{ij} \tag{17}$$

$$C_{ij} = -\frac{Mh}{2}\left[\frac{\sin(j\delta\varphi)}{i\delta\varphi}\overline{\delta_\varphi}(H^*)_{ij} - \cos(j\delta\varphi)\overline{\delta_\eta}(H^*)_{ij}\right] + \mathscr{Z}(w^*)_{ij} + h^2 \tag{18}$$

$$D_{ij} = -\frac{Mh}{2}\left[\frac{\sin(j\delta\varphi)}{i\delta\varphi}\overline{\delta_\varphi}(w^*)_{ij} - \cos(j\delta\varphi)\overline{\delta_\eta}(w^*)_{ij}\right] \tag{19}$$

where

$$b = \frac{\sqrt{Gr}}{2i}\overline{\delta_\eta}(\psi)_{ij}, \quad e = \frac{\sqrt{Gr}}{2i}\overline{\delta_\varphi}(\psi)_{ij},$$

$$\delta_\eta^2(\psi)_{ij} = \psi_{i+1j} - 2\psi_{ij} + \psi_{i-1j}$$

and

$$\overline{\delta_\eta}(\,)_{ij} = (\,)_{i+1j} - (\,)_{i-1j} \quad \overline{\delta_\varphi}(\,)_{ij} = (\,)_{ij+1} - (\,)_{ij-1}$$

and the operator $\mathscr{Z}(\,)_{ij}$ is defined as

$$\mathscr{Z}(\,)_{ij} = \frac{1}{12}\left[\frac{h^2}{\delta\varphi}(|e|-e)\left.\frac{\partial^2(\,)}{\partial\eta^2}\right|_{i+1j} + \frac{h^2}{\delta\varphi}(|e|+e)\left.\frac{\partial^2(\,)}{\partial\eta^2}\right|_{i-1j}\right] + \frac{1}{12}\left[\delta\varphi(b+|b|)\left.\frac{\partial^2(\,)}{\partial\varphi^2}\right|_{ij+1} - \delta\varphi(b-|b|)\left.\frac{\partial^2(\,)}{\partial\varphi^2}\right|_{ij-1}\right].$$

Equations (17)–(19) represent the source terms of their respective equations. (If the central difference scheme is used, the second terms of the coefficients A_1 and A_2, A_3 and A_4, F_1 and F_2, and F_3 and F_4 should be replaced by $e/(2\delta\varphi)$, $b/(2\delta\varphi)$, $e\,Pr/(2\delta\varphi)$, and $b\,Pr/(2\delta\varphi)$, respectively, but A_0 and F_0 would be just G_0. In addition, all $\mathscr{Z}(\,)$ operators would be dropped off from all equations.) Figure 2 shows the mesh arrangement where $i = 1, 2, \ldots, L-1$ and $j = 0, 1, \ldots, K$. Only the right half of the cross-section need be considered because the problem is symmetrical along the vertical diameter.

The discretized boundary conditions are given as

3.1. Vorticity boundary condition

$$\xi_L = \frac{3(\psi_L - \psi_{L-1})}{h^2} - \frac{\xi_{L-1}}{2}. \tag{20}$$

3.2. Dirichlet boundary conditions

$$\psi_{Lj} = 0 \quad w^*_{Lj} = 0 \quad H^*_{Lj} = 0. \tag{21}$$

3.3. Neumann boundary condition

$$\left.\frac{\partial\theta}{\partial\eta}\right|_{Lj} = 1 = \frac{-4\theta_{L-1j} + \theta_{L-2j} + 3\theta_{Lj}}{2h} + O(h^2). \tag{22}$$

4. Solution of the equations

The systems of linear algebraic equations can be solved by employing the line-iterative method with the procedure summarized as follows:

(1) Guess initial values for all the variables.
(2) Calculate w^*, H^* and θ at $\eta = 0$ using the rectangular form of the finite difference equations of those variables for next iteration.
(3) Apply Dirichlet boundary conditions, (21).
(4) Apply the condition that ψ and ξ are zero along the vertical diameter.
(5) Calculate ψ, ξ, w^* and H^* in the interior points using (12)–(15) for next cycle, keeping in mind that w^* and H^* are symmetrical along the vertical diameter.
(6) Apply boundary condition (20) for ξ.
(7) Calculate w from (6).
(8) Calculate θ in the interior points using (16), keeping in mind that θ is symmetrical along the vertical diameter.
(9) Apply the Neumann boundary condition, (22).
(10) Check the convergence by computing the root-mean-square residual, R_s, for each flow variable 's'. Convergence is considered to be achieved when $R_s < 10^{-4}$. R_s is defined from ref. [7], as

$$R_s = \sqrt{\sum_{i=0}^{L}\sum_{j=0}^{K}(s_{ij}^{n+1} - s_{ij}^{n})^2}.$$

(11) Repeat steps 2–10 until convergence is established.

5. Results

The simultaneous solution of equations (1)–(5) was first tested and compared to a number of known limiting cases. Setting the magnetic field and the buoyancy force terms equal to zero yielded the parabolic profile for pipe flow and the well known Nusselt number of 48/11 for forced convection with a constant heat flux at the wall. Letting both the buoyancy terms and the heat transfer to be zero but with non-zero magnetic field, the numerical results reproduced Gold's [8] MFM velocity profiles and nondimensional pressure gradient, γ. With constant heat flux at the wall, non-zero magnetic field and zero buoyancy forces, Gardner's [9] forced convection MFM solution was reproduced. Further numerical results where the buoyancy terms were included were tested for sensitivity to mesh size. Only convergent solutions were accepted. References [5, 6] discuss these comparisons in more detail. In general, a 24×24 mesh was used for Hartmann numbers up to 100. For larger values a 124×24 grid was employed in order to compute stable points in the Hartmann boundary layer. The machine used was a Micro-Vax II VMS system. The time required to achieve 100 iterations on a 24×24 mesh is about 1.7 min. The 124×24 grid required 8.35 min per 100 iterations. When the modified third-order accurate upwind scheme was used, the time for a 24×24 mesh was 3.1 min/100 iterations and 14.4 min/100 iterations for a 124×24 grid.

The combined axial flow and secondary flow caused by the natural convection creates a flow pattern in which the streamlines are in the form of a double helix as the fluid flows through the pipe. The fluid rises near the wall in the vicinity of $\phi = \pi/2$ where the axial flow is slow, moves up to the top of the pipe at $\phi = 0$ where it then flows downward through the middle of the cross-section where the axial flow is higher. Figure 3 shows streamlines in the plane of the cross-section for $Gr = 10^4$ and 10^6 and Hartmann numbers from 0–100. Figure 4 shows the up and down flow of the velocity profiles along the $\phi = \pi/2$ diameter. As the Hartmann number is increased the interaction of the field and the secondary flow is such that the secondary flow is suppressed. This is not a simple interaction because the secondary flow distorts the electric current lines as shown in Fig. 5. For large Grashof numbers ($\approx 10^6$) and low magnetic fields ($M = 1$), the electric current lines are distorted enough that they tend to close upon themselves in secondary loops as shown in the upper right-hand picture of Fig. 5.

Figure 6 shows how the natural convection and the magnetic field interact to distort the parabolic velocity profiles. As the Grashof number (natural convection) is increased, the secondary flow tends to slow the flow along the vertical diameter causing two maxima to appear. Increasing the Hartmann number (magnetic field) causes the symmetrical parabolic profile to change into a wedge shaped profile with the Hartmann flattening most prominent near the wall at $\phi = 0$ and $\phi = \pi$. The magnetic field also inhibits the spiral secondary flow and eliminates it entirely for large Hartmann numbers. Since the pipe wall

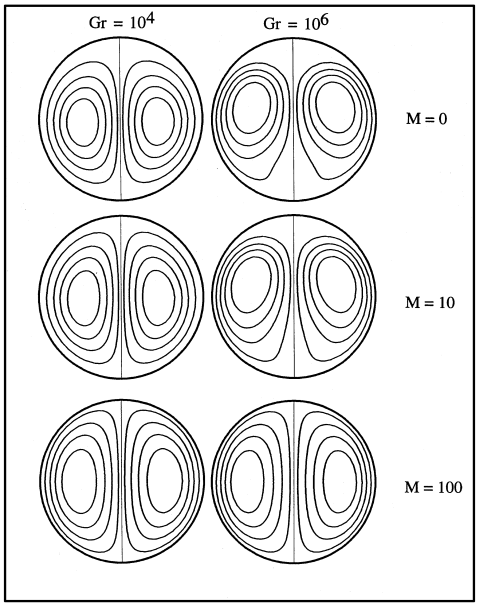

Fig. 3. Streamlines of the secondary flow as a function of the Grashof number and Hartmann number.

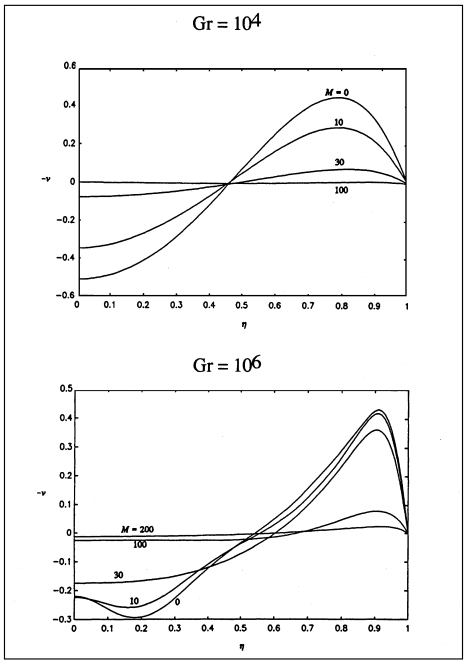

Fig. 4. Azimuthal velocity profiles at $\varphi = \pi/2$ as a function of Hartmann number and Grashof number.

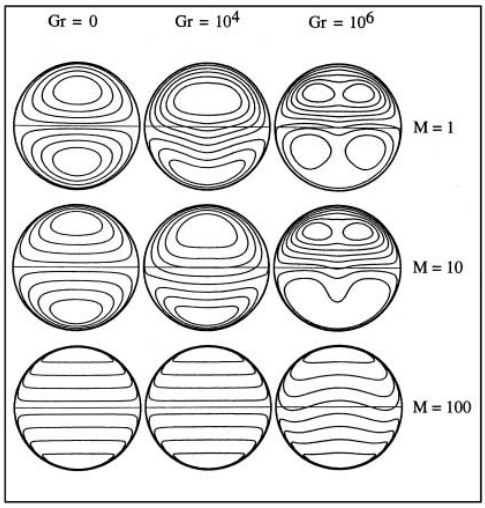

Fig. 5. Electric current lines as a function of the Grashof number and Hartmann number.

is assumed electrically insulated there is no net MFM ponderomotive force in the axial direction. The influence of the magnetic field and natural convection shows up in the local shear at the wall. This is apparent in Fig. 7 where the nondimensional pressure gradient is plotted as a function of the Hartmann and Grashof numbers, M and Gr, respectively. With increasing natural convection (Gr), the nondimensional pressure gradient increases. As the field is increased, the influence of the natural convection is diminished and all curves asymptotically approach Gold's solution [8] where natural convection is absent. The temperature profiles are displayed in Fig. 8 in the form of isotherms in the cross-section of the pipe. As the natural convection is increased, the isotherms are distorted from concentric circles to a 'fish mouth' pattern. With increasing magnetic field strength, the pattern reverts to a more symmetric circular pattern.

The secondary spiral motion of the natural convection induces an angular dependence into the problem influencing both velocity and temperature profiles. The Nusselt number, defined as $Nu = hd/k$, can be cast in terms of the wall heat flux as $Nu = qd/k(T_w - T_m)$ which depends on angular position through $T_w(\phi)$. The resulting angular dependence in the Nusselt number is shown in Figs 9 and 10. Figure 9, the case of zero field, demonstrates that the Nusselt number near the top of the pipe is reduced due to the fluid being heated as it rises along the side walls. The wall temperature increases in order to keep the wall heat flux constant and the temperature difference between the wall and the bulk mixing-cup temperature increases resulting in a decrease in Nusselt number. At the bottom of the cross-section the Nusselt number goes up because the temperature difference, $T_w - T_m$, is reduced by the cooler fluid coming into this region from the cooler central region of the cross-section. If the Grashof number is high (see $Gr = 10^6$ in Fig. 9), the secondary flow is strong enough to bring warmer fluid from the top of the cross-section all the way down to the wall region near $\phi = \pi$ causing the Nusselt number to reverse its trend and decrease. In Fig. 10 the influence of the magnetic field is shown over a range of Hartmann numbers of 0–500. As the field is increased, the Hartmann flattening dominates at $\phi = 0$ causing the Nusselt number to increase. At the bottom of the cross-section near $\phi = \pi$ the two mechanisms of damping of the natural convection and the Hartmann flattening compete with each other. For low Grashof numbers (10^4) the damping of the natural convection allows the Nusselt number to decrease monotonically. At the higher Grashof number (10^6) the Hartmann flattening first increases the Nusselt number and then as the natural convection is damped out, the Nusselt number decreases. As the natural convection is eliminated, the flow becomes symmetrical in each of the four quadrants of the cross-section. The complete picture of MFM natural convection is shown in Fig. 11 where the Nusselt number averaged over $\phi = 0$ to $\phi = \pi$ is plotted as a function of Hartmann and Grashof numbers. As the Grashof number is increased, the induced secondary flow increases the Nusselt number through the mechanism of bringing cooler fluid near the wall region. The maximum in the curve for $Gr = 10^6$ appears to be due to the fact that there is a range of values where both natural convection and Hartmann flattening act in concert to bring cooler fluid to the wall region. Eventually, as the magnetic field (Hartmann number) is increased further, the damping of the natural convection causes all curves to asymptotically approach the curve for MFM forced convection only [9]. The influence of natural convection can be considered insignificant at that point.

6. Summary

The problem of combined free and forced convection MFM pipe flow with a constant heat flux at the wall was solved numerically for a range of Grashof numbers from 0 to 10^6 and Hartmann numbers from 0 to 500. Velocity profiles, temperature profiles, local and average Nusselt numbers were presented showing a consistent picture that the application of the magnetic field inhibits the secondary motion of the natural convection while the velocity profile undergoes a metamorphosis from a parabolic profile to the wedge-shaped profile of MFM forced convection. The specific practical application of this information lies in being able to use it to determine the axial pressure gradient for pumping calculations and local and average heat transfer coefficients for heat transfer estimates in laminar pipe flows of electrically conducting fluids being subjected to applied external

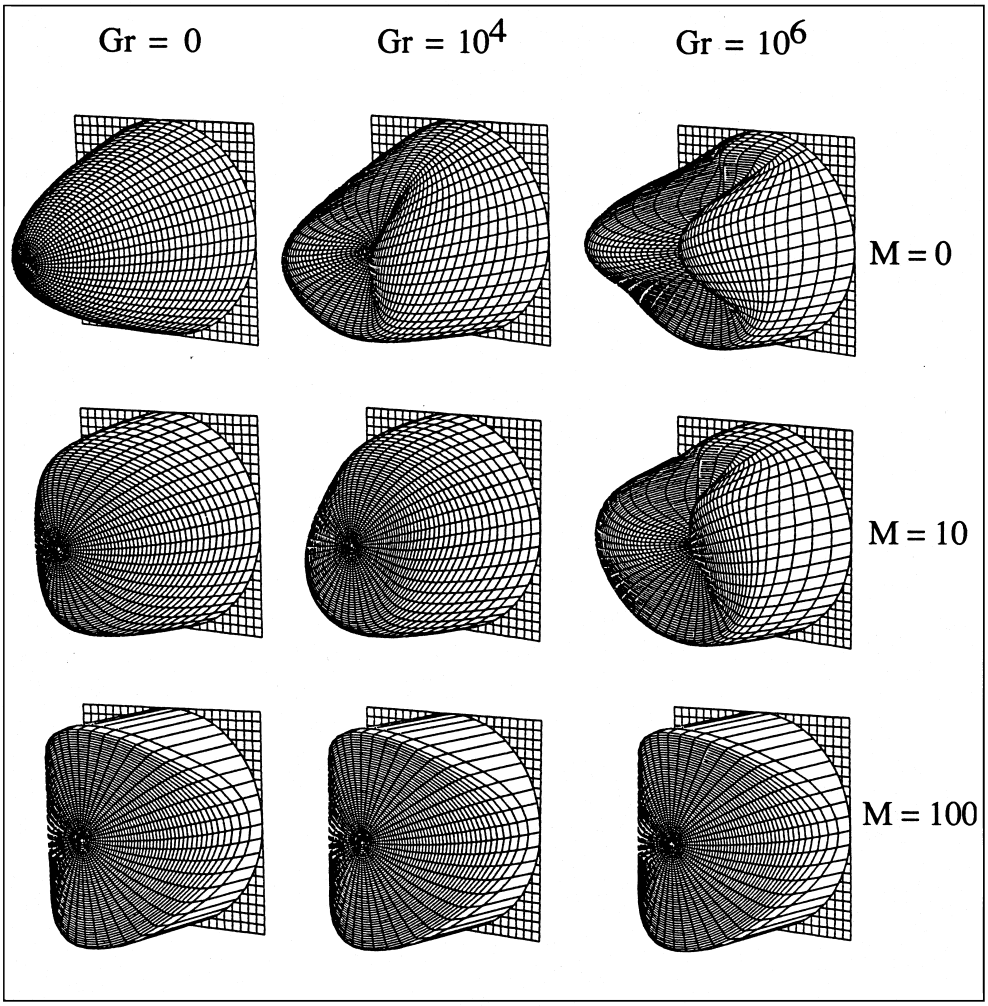

Fig. 6. Axial velocity profiles, $w(\eta, \varphi)$, as a function of Grashof number and Hartmann number.

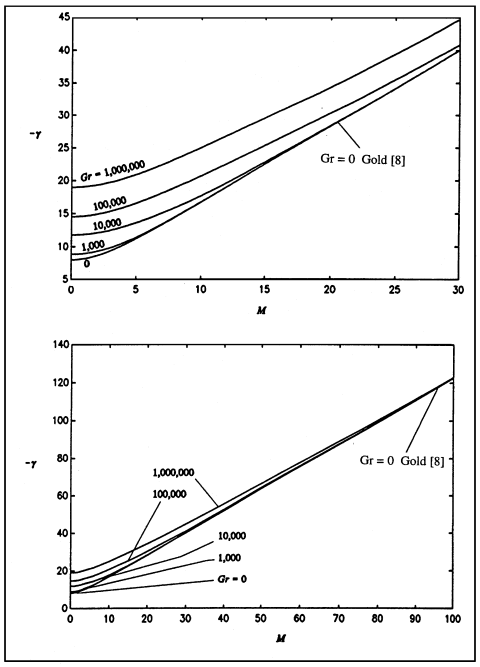

Fig. 7. Dimensionless pressure gradient for low and high Hartmann numbers.

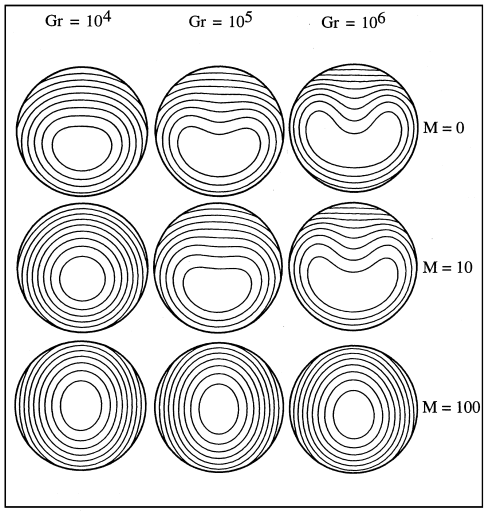

Fig. 8. Isotherms and nondimensional temperature as a function of Grashof number and Hartmann number.

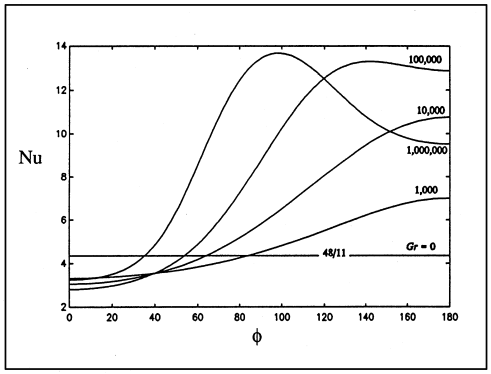

Fig. 9. Local Nusselt number as a function of Grashof number and angle from the vertical.

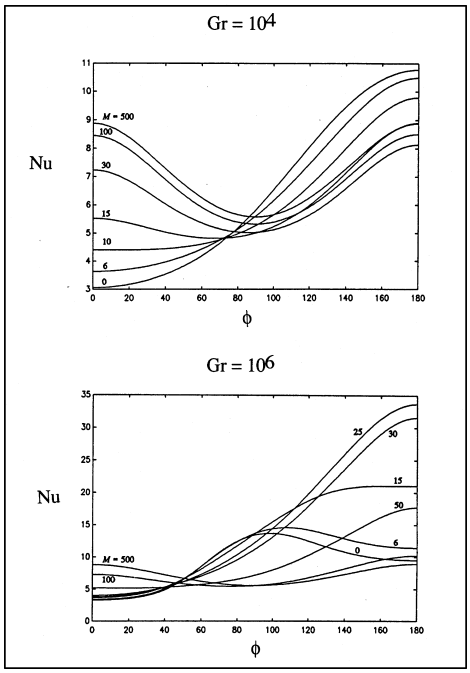

Fig. 10. Local Nusselt number as a function of angle from the vertical and Hartmann number for low and high Grashof numbers.

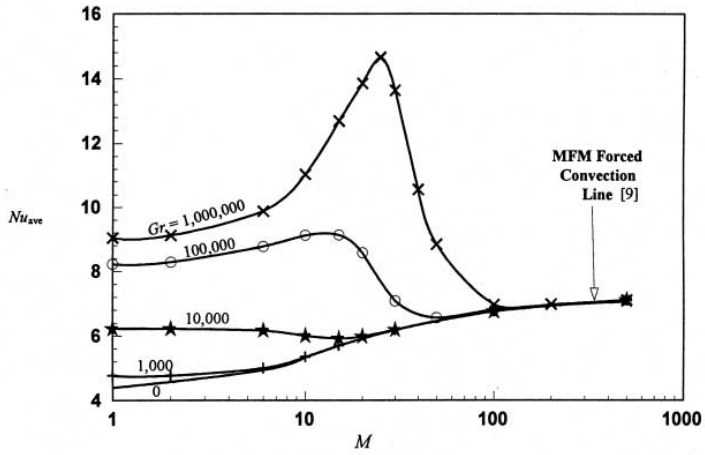

Fig. 11. Average Nusselt number as a function of Hartmann number and Grashof number. The symbols indicate values where complete numerical solutions were generated.

magnetic fields when both mechanisms of free and forced convection are important.

References

[1] H. Branover, Magnetohydrodynamic Flow in Ducts, Keter Publishing Jerusalem Ltd, Jerusalem, 1978.
[2] R.A. Gardner, P.S. Lykoudis, Magneto-fluid-mechanic pipe flow in a transverse magnetic field Part 1. Isothermal flow, J. Fluid Mech. 47 (1971) 737–764.
[3] Y.T. Lo, Combined free-and-forced convection in a transverse magnetic field, M.Sc. thesis, Washington University, St Louis, MO, 1973.
[4] R.A. Gardner, Y.T. Lo, Combined free-and-forced convection heat transfer in magneto fluid mechanic pipe flow, AIChE 73 (164) (1975) 133–141.
[5] M.J. Al-Khawaja, Numerical study of MFM free-and-forced convection pipe flow, D.Sc. thesis, Washington University, St Louis, MO, 1992.
[6] M.J. Al-Khawaja, R.A. Gardner, R.K. Agarwal, Numerical study of magneto-fluid-mechanic forced convection pipe flow, Engineering J. of Qatar University 7 (1994) 115–134.
[7] R.K. Agarwal, A third-order-accurate upwind scheme for Navier–Stokes solutions at high Reynolds numbers, AIAA Paper No. 81-0112, 1981.
[8] R. Gold, Magnetohydrodynamic pipe flow, Part 1, J. Fluid Mech. 13 (1962) 505.
[9] R.A. Gardner, Laminar pipe flow in a transverse magnetic field with heat transfer, Int. J. Heat Mass Transfer 11 (1968) 1076–1081.